Chemical Science

ROYAL SOCIETY OF CHEMISTRY

EDGE ARTICLE

View Article Online
View Journal



Cite this: DOI: 10.1039/d6sc01886f

All publication charges for this article have been paid for by the Royal Society of Chemistry

# Hybridized through-bond/through-space charge transfer enables efficient blue emitters with the Rec. 2020 color gamut

Xihao Yang,† Yongxu Hu,† Xiaoyu Guo, Jingsheng Miao, He Liu * and Chuluo Yang

Received 6th March 2026
Accepted 8th May 2026

DOI: 10.1039/d6sc01886f

rsc.li/chemical-science

Achieving efficient deep-blue emission with high color purity remains a critical challenge for BT.2020-compliant OLEDs. Herein, we present a rational molecular design strategy by tuning the hybridization between through-bond charge transfer (TBCT) and through-space charge transfer (TSCT) in a series of A1–D1–D2–A2 structured TADF emitters. Two proof-of-concept emitters, **BOtC** and **BOCC**, were synthesized with symmetric and asymmetric 1,1′-bicarbazole donors, respectively. Comprehensive theoretical and photophysical analyses reveal that **BOtC** exhibits balanced TBCT/TSCT hybridization, leading to a small energy difference ($\Delta E_{ST}$) between the first singlet ($S_1$) and triplet ($T_1$) excited states, fast reverse intersystem crossing, and efficient triplet exciton utilization. In contrast, TSCT-dominated **BOCC** shows slower RISC and reduced exciton recycling. Consequently, **BOtC**-based OLEDs achieve deep-blue emission (CIE: 0.157, 0.047) and a high external quantum efficiency (EQE) of 14.4%, whereas **BOCC**-based devices display a lower EQE of 6.5%. This work establishes TBCT/TSCT hybridization control as a general strategy to simultaneously achieve high efficiency and ultrahigh color purity in blue TADF emitters, providing guidance for next-generation display applications.



## Introduction

With the rapid demand of ultrahigh-definition display technologies, particularly for next-generation organic light-emitting diode (OLED) applications, the development of emissive materials capable of meeting the new Rec. 2020 color gamut standard has become an urgent priority.[1–3] Among the three primary colors, blue emitters remain the most challenging component due to their intrinsically high excited-state energies and limited stability. In particular, achieving efficient blue emission with Commission Internationale de l'Éclairage (CIE) coordinates approaching the Rec. 2020 blue point (0.131, 0.046) is still rare.[4–6] The scarcity of such emitters severely constrains the realization of wide-color-gamut OLED displays with high brightness, long operational lifetime, and low power consumption, thereby motivating intense research efforts toward molecular design strategies that simultaneously ensure color purity and high electroluminescence efficiency.

For purely organic emitters, thermally activated delayed fluorescence (TADF) emitters are regarded as highly promising candidates, and they can be broadly classified into conventional donor–acceptor (D–A) type TADF emitters[7–13] and multi-resonance (MR) TADF emitters.[14–24] Conventional D–A TADF emitters typically feature spatially separated highest occupied molecular orbitals (HOMOs) and lowest unoccupied molecular orbitals (LUMOs), resulting in a small singlet–triplet energy splitting ($\Delta E_{ST}$) and, consequently, an enhanced reverse intersystem crossing rate ($k_{RISC}$), which enables efficient harvesting of excitons. However, the pronounced charge-transfer character often induces significant structural relaxation in the excited state, leading to broad emission spectra with full width at half-maximum (FWHM) values generally exceeding 50 nm. To access the Rec. 2020 blue region with such broad-band emitters, substantial spectral blue-shifting is required, which typically necessitates the use of weak donor and acceptor moieties. This constraint dramatically limits the available molecular design.

In contrast, MR-TADF emitters, characterized by alternately positioned electron-deficient boron and electron-rich nitrogen or oxygen atoms within rigid polycyclic frameworks, exhibit highly localized frontier molecular orbitals (FMOs) and minimal geometrical relaxation upon excitation.[3,14] As a result, these emitters display narrow emission bands and small FWHM values, along with fast singlet radiative decay rates ($k_{r,S}$), making them particularly attractive for high-color-purity blue emission. Nevertheless, the atomically fixed electronic structures inevitably lead to substantial HOMO–LUMO overlap, which increases $\Delta E_{ST}$ and suppresses $k_{RISC}$, thereby limiting triplet exciton utilization.[25,26] Consequently, despite their excellent color purity, MR-TADF emitters often suffer from insufficient

*Shenzhen Key Laboratory of New Information Display and Storage Materials, College of Materials Science and Engineering, Shenzhen University, Shenzhen 518055, P. R. China. E-mail: liuhe001@szu.edu.cn*

† These authors contributed equally to this work.

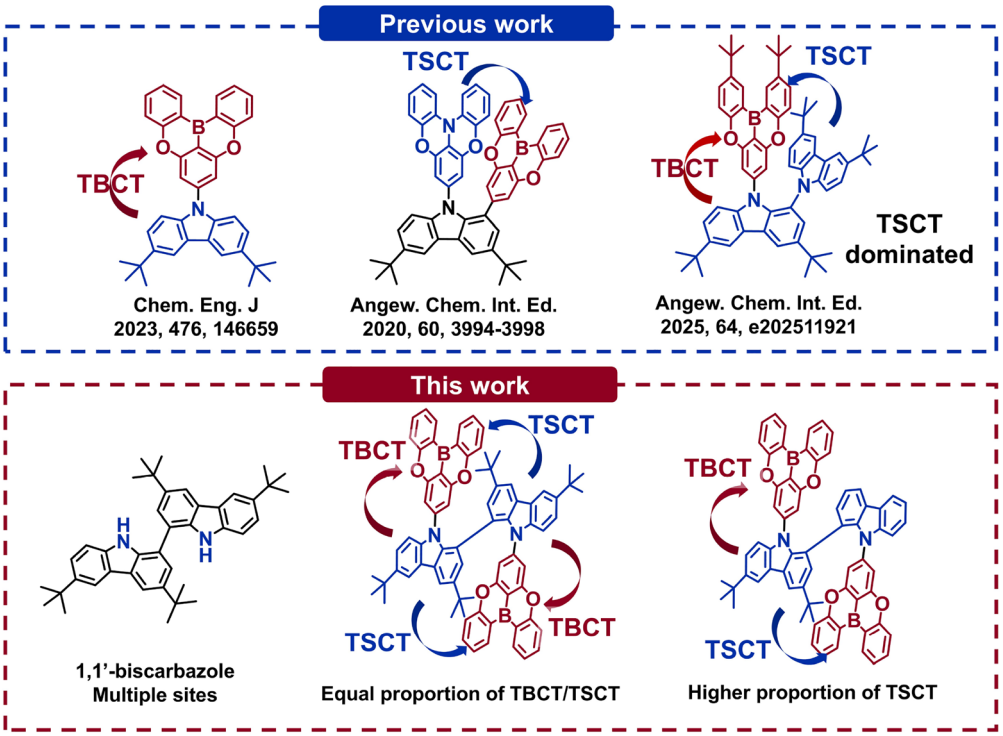


Fig. 1 Design principles of emitters with an even/uneven proportion of TBCT/TSCT hybridization.

electroluminescence efficiency. Overall, the rational design of TADF emitters that simultaneously deliver high efficiency and an ultralow CIE *y*-coordinate below 0.05 remains a formidable challenge in the field of organic optoelectronics.

The oxygen-embedded triarylboron (BO) moiety, featuring weak MR charge-transfer (MRCT) excitation, intrinsically delivers deep-blue emission accompanied by a fast $k_{r,S}$. Owing to these favorable photophysical characteristics, BO-based building blocks have been extensively employed in the construction of high-color-purity blue emitters.[27–37] Upon integration of a D unit, a long-range charge-transfer (LRCT) excited state can be introduced, which may partially hybridize with the MRCT state or even dominate the excited-state landscape. This hybridization effectively accelerates the reverse intersystem crossing process, leading to a substantially enhanced $k_{RISC}$, while largely preserving the fast $k_{r,S}$ and blue emission derived from the MR framework. To date, two major substitution strategies have been explored. One relies on twisted donor–acceptor architectures that promote through-bond charge transfer (TBCT),[27,28] whereas the other employs spatially proximate D–A arrangements enabling through-space charge transfer (TSCT).[35–40] In both approaches, the use of strong donor units—such as acridines[32] or indolocarbazoles[33,41]—or the deliberate introduction of pronounced steric hindrance to increase the donor–acceptor dihedral angle[29,33] generally stabilizes the first singlet excited state ($S_1$). This stabilization inevitably results in a red-shifted emission, yielding suboptimal color purity with $CIE_y$ coordinates typically exceeding 0.06. Conversely, the incorporation of weaker donors, such as carbazole derivatives, can better maintain deep-blue emission; however, the reduced CT character often leads to insufficient $k_{RISC}$ and incomplete triplet exciton harvesting.[42] Recent studies that synergistically combine TBCT and TSCT characteristics offer a promising avenue to reconcile these competing requirements by enabling fine-tuned excited-state hybridization.[43] Nevertheless, successful demonstrations remain scarce, underscoring the intrinsic difficulty of this molecular engineering challenge. Overall, the trade-offs among high electroluminescence efficiency, small $\Delta E_{ST}$, and ultrahigh color purity compliant with the BT.2020 standard persist, necessitating increasingly delicate and rational molecular design strategies.

Herein, we present a systematic investigation into the molecular design principles governing blue TADF emitters by deliberately modulating the hybridization proportion between through-bond charge transfer (TBCT) and through-space charge transfer (TSCT). Two proof-of-concept blue TADF emitters featuring an acceptor1–donor1–donor2–acceptor2 (A1–D1–D2–A2) architecture were rationally designed and synthesized (Fig. 1). By selectively controlling the substitution pattern of the 1,1′-bicarbazole core, the resulting emitters adopt either symmetric or asymmetric molecular configurations, thereby enabling distinct TBCT/TSCT hybridization behaviors. The symmetric molecule, 9,9′-di(5,9-dioxa-13b-boranaphtho[3,2,1-*de*]anthracen-7-yl)-3,3′,6,6′-tetra-*tert*-butyl-9H,9′H-1,1′-bicarbazole (**BOtC**), exhibits a balanced contribution of TBCT and TSCT from the donor units to the acceptors. In contrast, the asymmetric counterpart, 9,9′-di(5,9-dioxa-13b-boranaphtho[3,2,1-*de*]anthracen-7-yl)-3,6-di-*tert*-butyl-9H,9′H-1,1′-bicarbazole (**BOCC**), displays TSCT-dominated excited-state characteristics, primarily originating from the *tert*-butyl-

substituted carbazole donor toward both acceptor units. Despite their distinct excited-state hybridization profiles, both emitters exhibit similar deep-blue emission with identical peak maxima at 442 nm and comparably small ΔEST (0.07 eV for **BOtC** and 0.14 eV for **BOCC**). Notably, pronounced differences in exciton dynamics are observed. **BOtC** displays a significantly shorter delayed fluorescence lifetime ($\tau_d$) of 16.7 μs, compared to 28.8 μs for **BOCC**, indicative of a more efficient reverse intersystem crossing process. Accordingly, **BOtC** achieves a substantially higher $k_{RISC}$ of $1.36 \times 10^5$ $s^{-1}$, nearly double that of **BOCC** ($7.38 \times 10^4$ $s^{-1}$). These photophysical advantages directly translate into superior device performance. Electroluminescent devices based on **BOtC** deliver a maximum external quantum efficiency (EQE) of 14.4%, a current efficiency (CE) of 6.2 cd $A^{-1}$, and a maximum luminance ($L$) of 3000 cd $m^{-2}$, while maintaining a standard deep-blue emission with a $CIE_y$ coordinate of 0.047. This corresponds to a high blue index (BI) of 142 cd $A^{-1}$. In comparison, **BOCC**-based devices exhibit inferior performance, with a maximum EQE of 6.5%, a CE of 2.9 cd $A^{-1}$, an L of 2400 cd $m^{-2}$, and a BI of 67 cd $A^{-1}$. These results unequivocally demonstrate that fine-tuning the TBCT/TSCT hybridization ratio is a powerful strategy to simultaneously optimize exciton utilization and color purity in BT.2020-compliant blue TADF emitters.

## Results and discussion

### Molecular design and thermal and electrochemical properties

The emission characteristics of twisted D–A type TADF emitters are highly sensitive to the electronic nature of both D and A units. To access the deep-blue spectral region, both components must possess relatively weak donating or accepting strengths. Among various acceptor motifs, oxygen-embedded triarylboron (BO) has emerged as the most widely adopted building block owing to its rigid molecular framework, moderate electron-withdrawing capability, and, more importantly, its superior radiative efficiency arising from weak MR effects. However, the choice of D is also restricted, with carbazole- and acridine-based derivatives being the most commonly employed. Acridine derivatives are relatively strong electron donors and typically induce pronounced charge-transfer character, resulting in sky-blue emission with $CIE_y$ coordinates often exceeding 0.10. Carbazole derivatives, on the other hand, are weaker donors that help preserve deep-blue emission; however, the diminished charge-transfer interaction generally leads to a large $\Delta E_{ST}$, thereby limiting reverse intersystem crossing and inefficient triplet exciton utilization. Conventional strategies aimed at strengthening charge transfer—such as increasing the number of donor units or introducing substantial steric hindrance to enlarge the D–A dihedral angle—often lead to an undesired red-shift of the emission, counteracting gains in exciton utilization. To overcome these intrinsic limitations, TSCT has recently been incorporated into molecular design strategies. Notably, recent studies by Lu and co-workers demonstrated that hybridizing TBCT with TSCT can provide an effective balance between color purity and electroluminescent performance. Despite these encouraging results, the individual roles of TBCT and TSCT, as well as their cooperative interplay in governing excited-state dynamics remain insufficiently understood. To gain deeper insight into the underlying mechanisms, we conducted a systematic investigation focused on fine-tuning the relative contributions of TBCT and TSCT. In this design, 1,1′-bicarbazole featuring dual N–H functionalities was selected as the central donor scaffold to enable the attachment of two BO acceptor units, thereby allowing the simultaneous formation of multiple TBCT and TSCT pathways. Furthermore, the electron-donating strength of the 1,1′-bicarbazole core was precisely modulated through asymmetric *tert*-butyl substitution, providing a convenient handle to regulate the TBCT/TSCT hybridization ratio. The target emitters, **BOtC** and **BOCC**, were synthesized *via* conventional Buchwald–Hartwig coupling reactions and fully characterized by $^1H$ and $^{13}C$ NMR spectroscopy, mass spectrometry, and elemental analysis. Their thermal stability was evaluated using thermogravimetric analysis (TGA) and differential scanning calorimetry (DSC). As shown in Fig. S1, high thermal decomposition temperatures ($T_d$) of 424 °C were observed for both compounds. No distinct glass transition temperatures ($T_g$) were observed in the range of 50–300 °C, indicating excellent thermal stability and morphological stability.

### Crystal structure

To unambiguously confirm the molecular structure, single crystals of **BOtC** were successfully grown by slow evaporation from a mixed dichloromethane/methanol solution. The molecular and packing structures were determined by single-crystal X-ray diffraction analysis, which shows excellent agreement with the proposed chemical structure. As illustrated in Fig. 2, **BOtC** adopts a moderately twisted D–A conformation, with a torsion angle of 52° between the carbazole donor and BO acceptor units. This geometry suggests partial spatial decoupling of the FMOs, which is conducive to hybridization between LRCT and MRCT excited states, thereby favoring efficient radiative decay. Within the donor segment, the two carbazole units exhibit a dihedral angle of 54°, indicating a moderately twisted yet electronically coupled configuration that facilitates intramolecular charge communication. Meanwhile, the BO-based acceptor units engage in pronounced through-space interactions with the carbazole moieties, as evidenced by close π–π contacts with an intermolecular distance of approximately 3.5 Å. Such spatial proximity is expected to promote effective TSCT

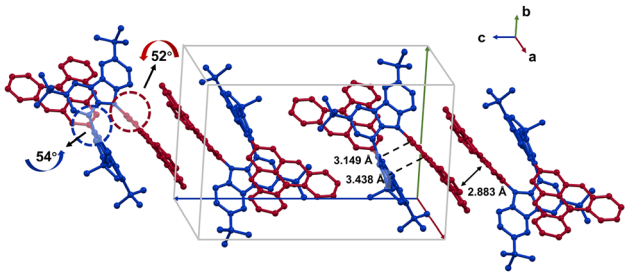


Fig. 2 Crystal structure of **BOtC** (CCDC: 2523284).

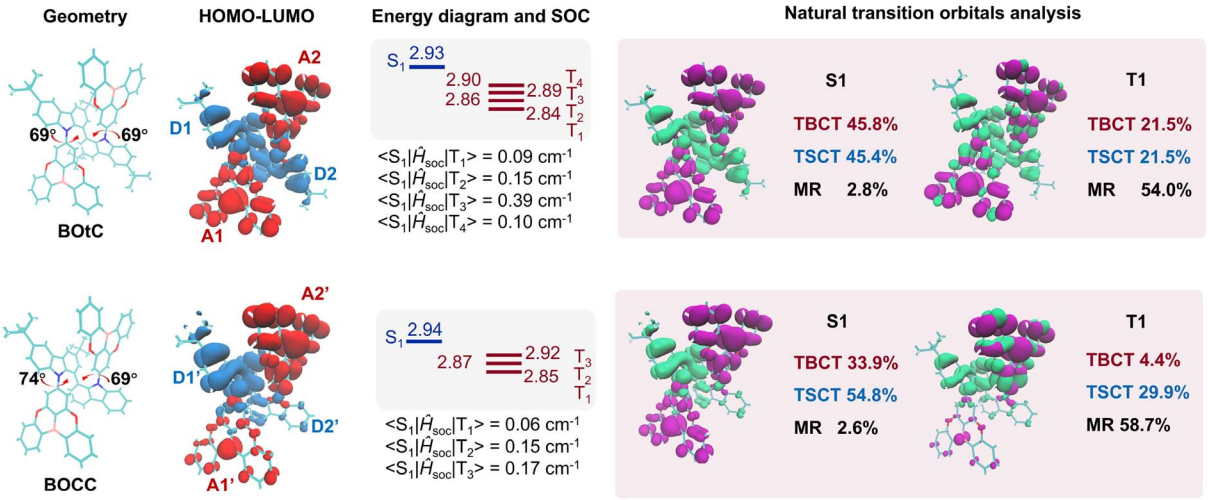


Fig. 3 Theoretical simulation result of **BOtC** and **BOCC**.

interactions, further contributing to excited-state hybridization. Notably, only weak C–H···π interactions are observed between BO and carbazole units within the crystal lattice, suggesting limited intermolecular electronic coupling. In contrast, acceptor–acceptor π–π stacking is detected outside the unit cell, with a short interplanar distance of 2.883 Å. This packing motif indicates that intermolecular aggregation is largely suppressed within the emissive core, which is advantageous for mitigating aggregation-induced quenching in the solid state. Importantly, both BO acceptor units adopt identical orientations relative to their attached carbazole donors, implying a symmetric electronic environment and comparable D–A interactions on both sides of the molecule. This structural symmetry could support the balanced TBCT/TSCT hybridization in **BOtC** and provide a solid structural basis for its favorable photophysical and electroluminescent performance.

## Theoretical simulation

To gain deeper insight into the optimized molecular geometries and ground-state electronic structures and to validate the proposed molecular design strategy, density functional theory (DFT) calculations were performed at the B3LYP/6-31G** level. As shown in Fig. 3, both **BOtC** and **BOCC** adopt comparable molecular geometries, featuring large torsion angles of approximately 70° between the BO acceptor and carbazole donor units. These dihedral angles are slightly larger than those observed in the single-crystal structure, which can be attributed to the absence of crystal-packing constraints in the gas-phase optimized geometries. Such moderately twisted conformations ensure partial spatial overlap between the HOMO and LUMO, a prerequisite for hybridized CT excited states. For both emitters, the LUMOs are predominantly localized on the BO acceptor units and exhibit clear MRCT characteristics, with electron density centered on the boron atom and the *ortho*- and *para*-carbon atoms of the adjacent phenyl rings. In **BOtC**, the LUMO is nearly evenly distributed over the two BO units (A1 and A2), indicative of a symmetric acceptor contribution. In contrast, **BOCC** shows a markedly asymmetric LUMO distribution, with dominant localization on the BO unit (A2′) connected to the carbazole without *tert*-butyl substitution, while the other BO unit (A1′) contributes less to the LUMO electron density. Distinct differences are also observed in the HOMO distributions. For **BOtC**, the HOMO is symmetrically delocalized across both carbazole donor units (D1 and D2), reflecting comparable donor strengths and electronic coupling. By contrast, the HOMO of **BOCC** is primarily localized on the *tert*-butyl-substituted carbazole (D1′), with significantly reduced electron density on the other carbazole unit (D2′). These asymmetric HOMO and LUMO distributions in **BOCC** strongly suggest an imbalanced donor–acceptor interaction. Collectively, **BOtC** exhibits a balanced hybridization of TBCT and TSCT, arising from the symmetric distribution of both the HOMO and LUMO. In contrast, **BOCC** displays a TSCT-dominated hybridized CT character due to its pronounced orbital asymmetry. Notably, the calculated LUMO energy levels are −1.75 eV for **BOtC** and −1.76 eV for **BOCC**, while the HOMO energy levels are −5.12 eV and −5.15 eV, respectively (Table 1), indicating that variations in TBCT/TSCT hybridization exert only a marginal influence on the absolute frontier orbital energy levels. Interestingly, a modest degree of spatial overlap between the HOMO and

Table 1 Theoretical simulation data of **BOtC** and **BOCC**

| Compound | HOMO (eV) | LUMO (eV) | $S_1$ (eV) | $T_1$ (eV) | $\Delta E_{ST}$ (eV) | $SOC_{S_1-T_1/2/3}$[a] ($cm^{-1}$) | $SOC_{S_1-T_4}$ ($cm^{-1}$) |
|---|---|---|---|---|---|---|---|
| **BOtC** | −5.12 | −1.75 | 2.93 | 2.84 | 0.09 | 0.09/0.15/0.39 | 0.10 |
| **BOCC** | −5.15 | −1.76 | 2.94 | 2.85 | 0.09 | 0.06/0.15/0.17 | — |

[a] $SOC_{S_1-T_1/2/3}$ refers to the spin–orbital coupling between $S_1$ and $T_1$ and $T_2$ and $T_3$, respectively.

LUMO is observed on the phenyl rings directly linked to the carbazole cores. This feature implies partial involvement of MRCT character in the excited states, which is expected to facilitate enhanced radiative decay rates and contribute to the fast singlet emission observed experimentally.

To further elucidate the nature of the excited-state configurations, natural transition orbital (NTO) analysis and inter-fragment charge transfer (IFCT) analysis were performed based on time-dependent DFT (TD-DFT) calculations. IFCT methods investigate how electrons are transferred between any two fragments of the system during the electronic excitation process. Taking **BOtC** as an example, we set four fragments to evaluate the electron transfer. Fragments 1 and 4 refer to the two BO acceptors and are marked as A1 and A2. Fragments 2 and 3 are the donors and named D1 and D2, respectively. The CT of D1 → A1 and D2 → A2 are through bond CT (TBCT), while D2 → A1 and D1 → A2 are through space CT (TSCT). Additionally, the CT located on A1 or A2 refers to the MR transition. Both **BOtC** and **BOCC** exhibit predominantly LRCT characteristics in their lowest singlet excited state ($S_1$), accompanied by only minor MRCT contributions of 2.8% and 2.6%, respectively. (Fig. S2 and S3) The key distinction between the two emitters arises from the relative contributions of TBCT and TSCT within the LRCT framework. For **BOtC**, the $S_1$ state comprises nearly equal contributions from TBCT (45.8%) and TSCT (45.8%), reflecting the symmetric donor–acceptor architecture and comparable electronic coupling pathways. In contrast, **BOCC** displays a pronounced TSCT-dominated character, with a TSCT contribution of 54.8% and a reduced TBCT component of 33.9%, originating from the more electron-rich donor unit (D1′) to the corresponding acceptors (A2′ and A1′). These results suggest that, in the asymmetric molecular configuration of **BOCC**, the enhanced donating capability of D1′ preferentially promotes TSCT over TBCT, highlighting the greater effectiveness of spatial charge transfer under such electronic asymmetry. Moreover, although the proportion of MRCT is small, it may accelerate the radiative decay to some extent. In the lowest triplet excited state ($T_1$), the MRCT component becomes dominant for both emitters, accounting for 54.0% in **BOtC** and 58.7% in **BOCC**. The calculated $S_1/T_1$ energy levels are 2.93/2.84 eV for **BOtC** and 2.94/2.85 eV for **BOCC**, respectively, resulting in a small $\Delta E_{ST}$ of approximately 0.09 eV. Such small $\Delta E_{ST}$ values are highly favorable for efficient RISC. Moreover, multiple triplet states are identified in close energetic proximity to their $S_1$, which can serve as additional intermediate channels to facilitate triplet up-conversion. To further evaluate the efficiency of intersystem crossing processes, the spin–orbit coupling (SOC) matrix elements between relevant triplet states and $S_1$ were calculated. **BOtC** exhibits slightly higher SOC values, with a maximum coupling strength of 0.39 $cm^{-1}$ between the $T_3$ and $S_1$ states, whereas **BOCC** shows a smaller maximum SOC value of 0.17 $cm^{-1}$. In addition, **BOtC** possesses an energy-closed $T_4$, which shows a SOC of 0.10 $cm^{-1}$. The combination of stronger SOC and a greater number of energetically accessible triplet states in **BOtC** strongly suggests a more efficient RISC process relative to **BOCC**. Overall, these theoretical analyses reveal distinct excited-state characteristics arising from different TBCT/TSCT hybridization patterns, providing a comprehensive understanding of the structure–property relationships that govern the TADF behavior and ultimately the divergent electroluminescent performance of the two emitters.

## Photophysical properties

To investigate how distinct electronic characteristics influence the photophysical behavior, UV-vis absorption and photoluminescence (PL) measurements were performed in dilute toluene solutions and in doped films (10 wt% in dibenzo[*b*,*d*]furan-2,8-diylbis(diphenylphosphine oxide), PPF). As shown in Fig. 4a, both emitters display intense absorption bands below 310 nm, which are attributed to π–π* transitions of the donor moieties. The broad absorption features spanning 320–360 nm originate from n–π* transitions associated with the carbazole units, while the absorption band centered at around 370 nm corresponds to the characteristic π–π* transition of the BO acceptor. Notably, no distinct intramolecular CT absorption bands are observed, suggesting weak ground-state CT interactions. In dilute solution, both **BOtC** and **BOCC** exhibit structureless and broad PL emission profiles with maxima at 425 nm, a hallmark of CT-dominated excited states, confirming the LRCT nature of their emissive states. In doped films, **BOtC** and **BOCC** show blue emission with single emission peaks at 441 nm and 436 nm, respectively. Considering that **BOCC** contains fewer *tert*-butyl substituents and therefore possesses weaker resistance to intermolecular aggregation, the observed blue-shifted emission of **BOCC** is primarily attributed to differences in excited-state hybridization patterns rather than

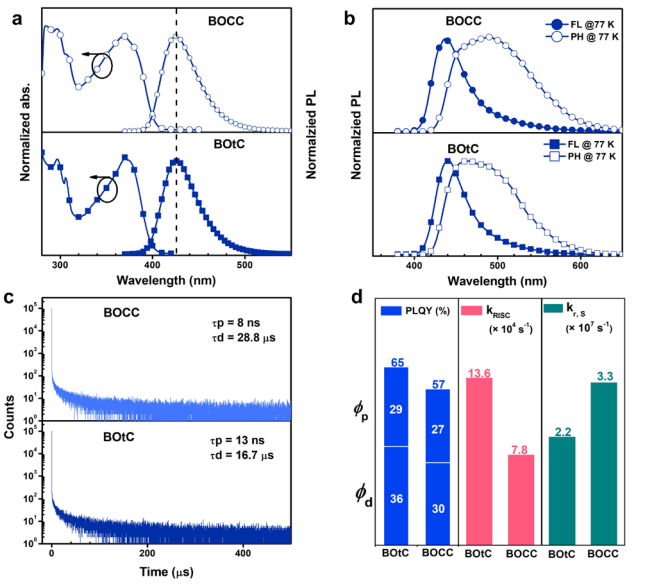


Fig. 4 Photophysical properties of BOtC and BOCC. (a) Absorption and photoluminescence in dilute toluene ($10^{-5}$ M). (b) Fluorescence and phosphorescence in doped films (10 wt% in PPF) at 77 K. (c) Transient PL decay profiles in doped films (10 wt% in PPF) under an oxygen free environment. (d) Comparison of the key parameters: PLQY, $k_{RISC}$ and $k_{r,S}$.

aggregation effects. Based on the onsets of fluorescence (Fl) and phosphorescence (Ph) spectra, the singlet and triplet energy levels ($E_{S_1}/E_{T_1}$) are estimated to be 3.00/2.93 eV for **BOtC** and 3.04/2.90 eV for **BOCC**, respectively. The slightly higher $E_{S_1}$ value observed for **BOCC** further indicates that the TBCT/TSCT hybridization pattern exerts a measurable influence on excited-state energetics. Consequently, the $\Delta E_{ST}$ values are determined to be 0.07 eV for **BOtC** and 0.14 eV for **BOCC**, both sufficiently small to enable effective triplet harvesting *via* RISC. The phosphorescence spectra of the respective donors and acceptor motifs were also recorded and are shown in Fig. S5. The triplet energy levels of these units are calculated to be 3.10 eV for BO, 2.94 eV for 2tCz (donor of **BOtC**) and 2.88 eV for tCzCz (donor of BOC). The slightly larger $\Delta E_{ST}$ of **BOCC** could be ascribed to the lower triplet energy of its donor unit. Overall, the similar absorption and emission characteristics of the two emitters suggest that CT interactions predominantly occur between the *tert*-butyl-substituted carbazole and BO units, while the relative TBCT/TSCT ratios subtly modulate excited-state properties. Moderate photoluminescence quantum yields (PLQYs) of 65% for **BOtC** and 57% for **BOCC** are obtained in doped films, which can be attributed to the intrinsic flexibility of the molecular frameworks.

To further elucidate exciton decay dynamics, transient PL decay measurements were carried out for doped films (10 wt% in PPF). As shown in Fig. 4c, both emitters exhibit distinct prompt fluorescence (PF) and delayed fluorescence (DF) components, characteristic of TADF behavior. The decay profiles are well fitted using a bi-exponential model, yielding PF lifetimes ($\tau_p$) of 13 ns for **BOtC** and 8 ns for **BOCC**, along with DF lifetimes ($\tau_d$) of 16.7 μs and 28.8 μs, respectively (Table 2). The PF-to-DF contribution ratios ($R_p/R_d$) are determined to be 44%/56% for **BOtC** and 47%/53% for **BOCC** (Fig. 4d), indicating differences in exciton recycling efficiency. By combining PLQY data with the transient decay results, key kinetic parameters—including the $k_{r,S}$, intersystem crossing rate ($k_{ISC}$), and $k_{RISC}$—were extracted (Table 2). **BOtC** exhibits a shorter $\tau_d$ and a slightly higher DF contribution than **BOCC**, resulting in a significantly enhanced $k_{RISC}$ of $1.36 \times 10^5$ $s^{-1}$, accompanied by a modestly reduced $k_{r,S}$ of $2.2 \times 10^7$ $s^{-1}$. In contrast, the prolonged $\tau_d$ of **BOCC** corresponds to a lower $k_{RISC}$ of $0.74 \times 10^5$ $s^{-1}$, despite a higher $k_{r,S}$ of $3.35 \times 10^7$ $s^{-1}$. These results clearly demonstrate that excited states with different TBCT/TSCT hybridization ratios exhibit markedly different efficiencies in triplet exciton recycling. Specifically, the balanced TBCT/TSCT hybridization in **BOtC** enables rapid RISC, with a $k_{RISC}$ value approximately 84% higher than that of **BOCC**. This behavior may originate from the formation of the $S_1$ state: in **BOtC**, both carbazole donors actively participate in CT interactions, contributing 45.8% TBCT (D1 → A1 and D2 → A2) and 45.4% TSCT (D1 → A2 and D2 → A1). In contrast, the $S_1$ state of **BOCC** is dominated by a single *tert*-butyl-substituted carbazole donor, giving rise to 33.9% TBCT (D1′ → A1′) and 54.8% TSCT (D1′ → A2′). The necessity for one donor to supply electrons to two acceptors in **BOCC** could weaken the effective CT interaction, consistent with its slightly blue-shifted emission and reduced $k_{RISC}$. Additionally, the slightly larger $\Delta E_{ST}$ could also contribute to the slow RISC of **BOCC**. Taken together, these comprehensive photophysical analyses not only confirm the excellent TADF characteristics of **BOtC** and **BOCC**, but also unambiguously reveal how finely tuning TBCT/TSCT hybridization governs excited-state decay pathways, thereby dictating triplet exciton utilization efficiency in deep-blue TADF emitters.

## EL performance

To further evaluate the impact of such excited states on their EL performance, devices with the following structures ITO/HATCN (5 nm)/TAPC (30 nm)/TCTA (15 nm)/mCBP (10 nm)/PPF:emitters (20–30 wt%, 25 nm)/PPF (20 nm)/LET006 (30 nm)/Liq/Al were fabricated. HATCN (1,4,5,8,9,11-hexaazatriphenylene hexacarbonitrile) was the hole-injection layer; TAPC (1,1-bis[(di-4-tolylamino)phenyl] cyclohexane) and TCTA (tris(4-carbazolyl-9-ylphenyl)amine) functioned as hole-transporting layers; thin layers of mCBP (3,3′-bis(carbazol-9-yl) biphenyl) and PPF were chosen as the electron- and hole-blocking layer; LET006 (2-ethyl-1-(4-(10-(naphthalen-2-yl) anthracen-9-yl)phenyl)-1H-benzo[*d*]imidazole) served as the electron-transporting layer. The emitting layer (EML) is composed of a PPF host and **BOtC** and **BOCC** at 10–30 wt%, respectively. The EL profiles are shown in Fig. 5 and S6–9, and the data are summarized in Table 3 and S2.

First, the doping concentration was optimized using **BOtC** as the emissive dopant. Devices fabricated with three different doping levels all exhibit single-peaked blue electroluminescence (EL) spectra with emission maxima at 434–439 nm, confirming effective exciton confinement on the **BOtC** molecules. The FWHM remains constant at ≈45 nm across all devices, resulting in excellent color purity with $CIE_y$ coordinates ranging from 0.041 to 0.050, well aligned with the BT.2020 blue standard. As the doping concentration increases from 10 wt% to 20 wt%, only a slight spectral shift is observed, indicating a reasonable resistance to aggregation for **BOtC**. Meanwhile, the turn-on voltage ($V_{on}$) decreases to 3.6 V at 20 wt%, suggesting that the increased dopant concentration facilitates improved charge transport within the emitting layer. **BOtC**-based devices achieve optimal performance at a doping concentration of 20 wt%, delivering a maximum external quantum efficiency

Table 2 Data of transient PL decay of **BOtC** and **BOCC** in doped films (10 wt% in PPF)

| Emitter | $\tau_p$ (ns) | $\tau_d$ (μs) | $\Phi_{PL}$ (%) | $\Phi_p$ (%) | $\Phi_d$ (%) | $k_{r,s}$ ($10^7$ $s^{-1}$) | $k_{ISC}$ ($10^7$ $s^{-1}$) | $k_{RISC}$ ($10^5$ $s^{-1}$) | $k_{nr}$ ($10^7$ $s^{-1}$) |
|---|---|---|---|---|---|---|---|---|---|
| **BOtC** | 13 | 16.7 | 65 | 29 | 36 | 2.20 | 4.31 | 1.36 | 1.19 |
| **BOCC** | 8 | 28.8 | 57 | 27 | 30 | 3.35 | 6.63 | 0.74 | 2.53 |

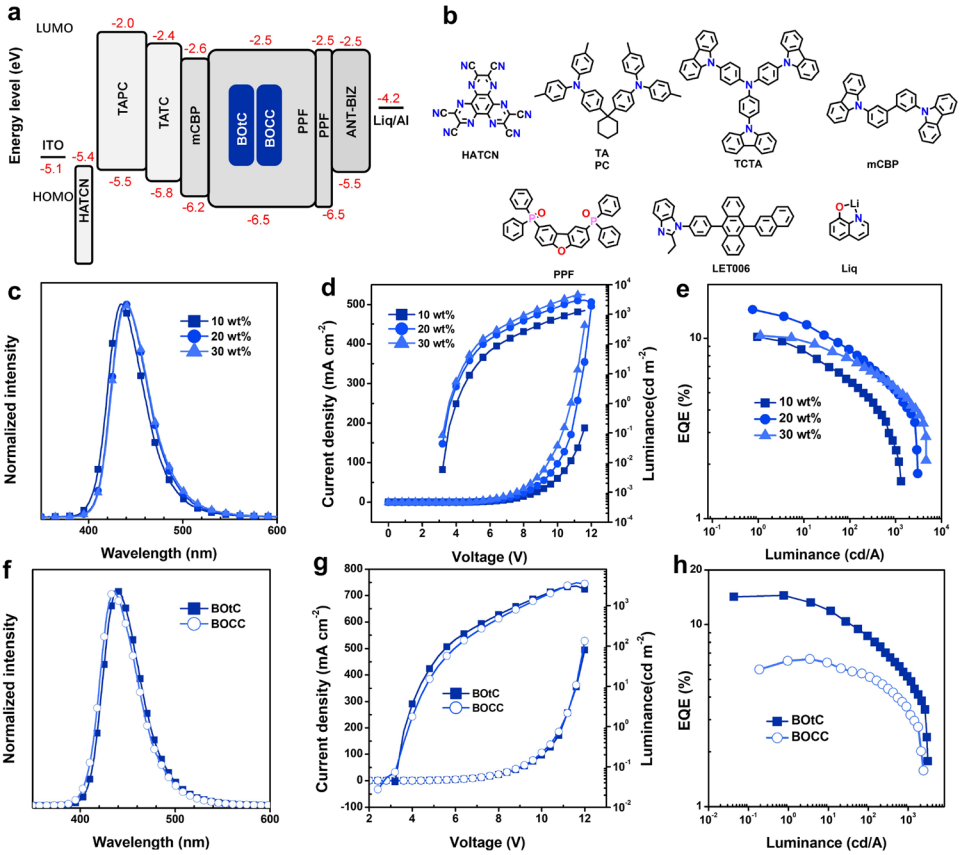


Fig. 5 Electroluminescent properties of TADF-OLEDs using **BOtC** and **BOCC** as emitters with different doping concentrations. (a) Energy diagram. (b) Chemical structure of materials used in devices. (c) EL spectra of **BOtC** based devices, (d) *J*–*V*–*L* curves **BOtC** based devices, (e) EQE *vs. L* profiles of **BOtC** based devices, (f) comparison of EL spectra of **BOtC** and **BOCC** based devices, (g) comparison of *J*–*V*–*L* curves of **BOtC** and **BOCC** based devices, and (h) comparison of EQE *vs. L* profiles of **BOtC** and **BOCC** based devices.

(EQE) of 14.4%, compared with ≈10% EQE at both 10 wt% and 30 wt%. The moderate EQEs at lower and higher doping levels can be attributed to limited PLQY and dopant aggregation, respectively. The improvement in EQE from 10 wt% to 20 wt% is primarily associated with enhanced carrier balance, whereas the efficiency-drop at 30 wt% likely arises from aggregation-induced nonradiative decay. Consistently, the highest current efficiency (CE) of 6.7 cd $A^{-1}$ is obtained at 20 wt%, corresponding to a high blue index (BI) of 142 cd $A^{-1}$. To elucidate the impact of different TBCT/TSCT hybridization patterns on EL performance, **BOCC**-based devices were subsequently evaluated at a doping concentration of 20–30 wt% (Fig. S8). The emission spectra remain essentially unchanged, with a slightly blue-shifted peak at 436 nm and a narrow FWHM of 44 nm, yielding CIE coordinates of (0.154, 0.043), which are also close to the BT.2020 blue region. The maximum luminance is slightly enhanced at higher doping levels; however, the maximum EQE remains limited at approximately 6.5–6.6%, showing little dependence on doping concentration. Assuming a similar light out-coupling efficiency to **BOtC**-based devices, the theoretical maximum EQE of **BOCC** is estimated to be 12.6% based on its PLQY of 57%. The substantial discrepancy between the theoretical and experimental EQEs suggests pronounced non-radiative exciton losses during device operation. This limitation is likely associated with the relatively slow RISC process, which hinders efficient triplet exciton harvesting, leading to exciton accumulation and subsequent quenching pathways. Overall, these results indicate that simply increasing the doping

Table 3 EL data of the sensitized devices based on **BOtC** and **BOCC**

| EML | $\lambda_{EL}$ (nm) | $L_{max}$ (cd $m^{-2}$) | $V_{on}$ (V) | $CE_{max}$ (cd $A^{-1}$) | $EQE_{max/100}$ (%) | BI (cd $A^{-1}$) | CIE ($x$, $y$) |
|---|---|---|---|---|---|---|---|
| 10% **BOtC** | 435 | 1314 | 4.0 | 4.2 | 10.2/5.7 | 102 | (0.154, 0.041) |
| 20% **BOtC** | 439 | 3049 | 3.6 | 6.7 | 14.4/8.6 | 142 | (0.153, 0.047) |
| 30% **BOtC** | 439 | 4637 | 3.6 | 5.9 | 10.0/7.6 | 118 | (0.152, 0.050) |
| 20% **BOCC** | 436 | 2408 | 4.4 | 2.9 | 6.5/5.2 | 67 | (0.154, 0.043) |
| 30% **BOCC** | 435 | 3663 | 4.0 | 3.2 | 6.6/5.4 | 68 | (0.154, 0.047) |

concentration does not effectively improve the exciton utilization efficiency of **BOCC**. More importantly, they highlight that a balanced TBCT/TSCT hybridization is superior to TSCT-dominated architectures with multiple acceptors for achieving both high color purity and high electroluminescence efficiency in deep-blue OLEDs.

The efficiency roll-off of both devices was further analyzed by fitting the experimental EQE–current density (EQE–*J*) curves using a triplet–triplet annihilation (TTA) model, together with singlet-involved quenching models, including singlet–triplet annihilation (STA) and singlet–polaron annihilation (SPA). As shown in Fig. 6 and S9, the roll-off behavior of **BOtC**-based devices follows the TTA model well at low current densities, corresponding to a luminance of approximately 350 cd $m^{-2}$. At higher current densities, noticeable deviations from the TTA model emerge, while the STA and SPA models also show increasing discrepancies, suggesting that multiple quenching pathways coexist at high exciton densities. The relatively good agreement with the STA model at the initial stage indicates that singlet–triplet interactions may contribute to the early efficiency roll-off. This behavior is likely associated with the bulky molecular structure and relatively fast RISC process of **BOtC**, which helps recycle triplet excitons but may not completely suppress exciton–exciton or exciton–polaron interactions at elevated current densities. In contrast, **BOCC**-based devices exhibit better agreement with the TTA model over a broader current density range, particularly at higher current densities, while the SPA model shows significant deviations across the entire range. Deviations observed below 50 mA $cm^{-2}$, together with partial agreement with the STA model, imply the involvement of additional singlet-related quenching pathways. At higher current densities, TTA becomes the dominant quenching mechanism, which is consistent with the relatively slower RISC process in **BOCC** leading to greater triplet accumulation. Overall, these results indicate that both singlet- and triplet-related quenching processes contribute to the efficiency roll-off. A well-balanced TBCT/TSCT hybridization not only enhances exciton utilization efficiency but also helps mitigate efficiency roll-off by regulating exciton dynamics, underscoring its importance in the design of high-performance BT.2020-compliant blue TADF emitters.

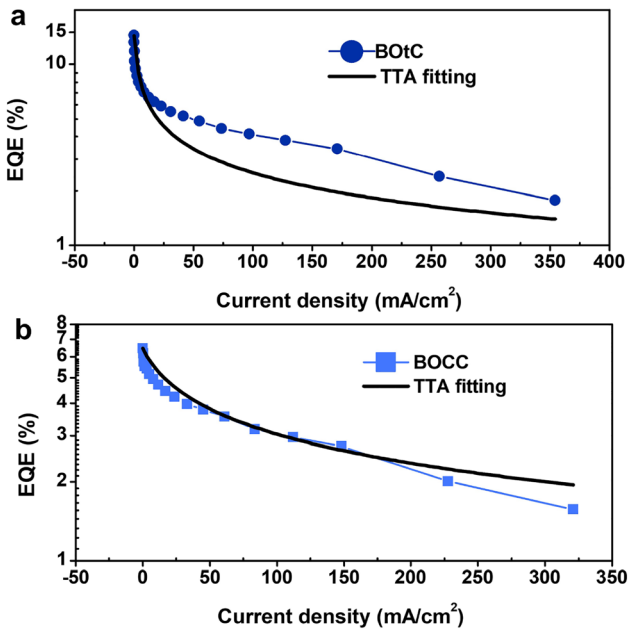


Fig. 6 The EQE–*J* curves and the fitting lines of TTA for **BOtC** (a) and **BOCC** (b) at a doping concentration of 20 wt%.

To further evaluate the potential of these emitters as TADF sensitizers, sensitized OLED devices were fabricated using **BOtC** as the sensitizer and *ν*-DABNA as the terminal emitter (Fig. S10). Considering its higher device efficiency and more favorable exciton dynamics compared with **BOCC**, **BOtC** was selected as the sensitizer in this study. The sensitized device exhibits a sharp EL spectrum characteristic of *ν*-DABNA, indicating efficient energy transfer from the **BOtC** sensitizer to the narrowband emitter. The device achieves a maximum luminance of 6454 cd $m^{-2}$ and a peak EQE of 25.9%, both higher than those of the corresponding **BOtC**-doped devices. Notably, the efficiency roll-off is significantly suppressed, with the EQE remaining at 20% at 100 cd $m^{-2}$ and 13.4% at 1000 cd $m^{-2}$. These results suggest that **BOtC** can function effectively as a TADF sensitizer and highlight the potential advantages of the sensitizing strategy for achieving high-efficiency and low roll-off OLED devices.

## Conclusions

In summary, we have systematically elucidated the role of TBCT and TSCT hybridization in governing the excited-state dynamics and electroluminescent performance of deep-blue TADF emitters. By rationally designing two proof-of-concept emitters with an A1–D1–D2–A2 architecture and precisely tuning the electronic asymmetry of the 1,1′-bicarbazole donor through *tert*-butyl substitution, we successfully modulated the relative contributions of TBCT and TSCT while retaining identical acceptor frameworks. Comprehensive structural, theoretical, and photophysical investigations reveal that the symmetric emitter **BOtC** exhibits a well-balanced TBCT/TSCT hybridization, leading to small $\Delta E_{ST}$, enhanced spin–orbit coupling, and RISC. In contrast, the asymmetric **BOCC** features a TSCT-dominated excited-state character, which weakens effective charge transfer, slows RISC, and limits triplet exciton utilization. These intrinsic differences directly translate into divergent exciton dynamics and device performances. As a result, **BOtC**-based OLEDs deliver high efficiency with a maximum EQE of 14.4%, a high BI of 142 cd $A^{-1}$, and excellent color purity with a CIE *y* coordinate as low as 0.047, closely satisfying the BT.2020 blue standard. Moreover, the balanced hybridization effectively suppresses efficiency roll-off by mitigating triplet accumulation through rapid RISC. In contrast, **BOCC**-based devices suffer from pronounced efficiency loss. This work not only provides a clear mechanistic understanding of how TBCT and TSCT cooperatively regulate excited-state formation, decay pathways, and exciton recycling, but also establishes balanced TBCT/TSCT hybridization as a powerful and general molecular design strategy for achieving high-efficiency, ultrahigh-color-purity

blue TADF emitters. These insights are expected to guide the future development of next-generation organic emitters toward practical BT.2020-compliant OLED applications.

## Author contributions

X. Yang, Y. Hu, and X. Guo: conceptualization, data curation, formal analysis, methodology, investigation, J. Miao: formal analysis, methodology, supervision, H. Liu: conceptualization, formal analysis, funding acquisition, methodology, software, supervision, validation, writing – original draft, writing – review & editing, and C. Yang: funding acquisition, supervision, writing – review & editing.

## Conflicts of interest

There are no conflicts to declare.

## Data availability

CCDC 2523284 contains the supplementary crystallographic data for this paper.[44]

All relevant data are either included in the main text or in the supplementary information (SI). Supplementary information: experimental details, thermal properties, DFT calculations, phosphorescent spectra, electroluminescent profiles, single crystal data, NMR spectra and references. See DOI: https://doi.org/10.1039/d6sc01886f.

## Acknowledgements

This work was supported by the National Natural Science Foundation of China (No. 52373191 and 52130308), the Guangdong Basic and Applied Basic Research Foundation (2023A1515030176, 2023A1515110356), the Shenzhen Science and Technology Program (JCYJ20240813142905007 and ZDSYS20210623091813040), and the Research Team Cultivation Program of ShenZhen University (No. 2023DFT004). We thank the Instrumental Analysis Center of Shenzhen University for analytical support.

## References

1 C.-Y. Chan, M. Tanaka, Y.-T. Lee, Y.-W. Wong, H. Nakanotani, T. Hatakeyama and C. Adachi, *Nat. Photonics*, 2021, **15**, 203–207.
2 S. O. Jeon, K. H. Lee, J. S. Kim, S.-G. Ihn, Y. S. Chung, J. W. Kim, H. Lee, S. Kim, H. Choi and J. Y. Lee, *Nat. Photonics*, 2021, **15**, 208–215.
3 Y. Kondo, K. Yoshiura, S. Kitera, H. Nishi, S. Oda, H. Gotoh, Y. Sasada, M. Yanai and T. Hatakeyama, *Nat. Photonics*, 2019, **13**, 678–682.
4 T. Hua, X. Cao, J. Miao, X. Yin, Z. Chen, Z. Huang and C. Yang, *Nat. Photonics*, 2024, **18**, 1161–1169.
5 S. Q. Zhang, Z. L. Cheng, H. Wu, T. Y. Zhang, Y. L. Yang, J. Li, Y. C. Cheng, J. Yu, Y. Z. Shi, X. C. Fan, K. Wang and X. H. Zhang, *Adv. Mater.*, 2026, **38**, e17512.
6 Y. Wang, X. Guo, J. Bian, Z. Ma, X. Ge, L. Jiang, G. Li, Z. Chen, D. Guo, J. Zhao, Z. Yang, J. Miao and Z. Chi, *Adv. Mater.*, 2026, **38**, e14617.
7 H. Uoyama, K. Goushi, K. Shizu, H. Nomura and C. Adachi, *Nature*, 2012, **492**, 234–238.
8 Q. Zhang, B. Li, S. Huang, H. Nomura, H. Tanaka and C. Adachi, *Nat. Photonics*, 2014, **8**, 326–332.
9 T. A. Lin, T. Chatterjee, W. L. Tsai, W. K. Lee, M. J. Wu, M. Jiao, K. C. Pan, C. L. Yi, C. L. Chung, K. T. Wong and C. C. Wu, *Adv. Mater.*, 2016, **28**, 6976–6983.
10 W. Zeng, H. Y. Lai, W. K. Lee, M. Jiao, Y. J. Shiu, C. Zhong, S. Gong, T. Zhou, G. Xie, M. Sarma, K. T. Wong, C. C. Wu and C. Yang, *Adv. Mater.*, 2018, **30**, 1704961.
11 L. Gan, Z. Xu, Z. Wang, B. Li, W. Li, X. Cai, K. Liu, Q. Liang and S. J. Su, *Adv. Funct. Mater.*, 2019, **29**, 1808088.
12 M. R. Bryce, C. Li, A. K. Harrison, Y. Liu, Z. Zhao, C. Zeng, F. B. Dias, Z. Ren and S. Yan, *Angew. Chem., Int. Ed.*, 2021, **61**, e202115140.
13 H. Liu, Z. Liu, G. Li, H. Huang, C. Zhou, Z. Wang and C. Yang, *Angew. Chem., Int. Ed.*, 2021, **60**, 12376–12380.
14 T. Hatakeyama, K. Shiren, K. Nakajima, S. Nomura, S. Nakatsuka, K. Kinoshita, J. Ni, Y. Ono and T. Ikuta, *Adv. Mater.*, 2016, **28**, 2777–2781.
15 M. Yang, I. S. Park and T. Yasuda, *J. Am. Chem. Soc.*, 2020, **142**, 19468–19472.
16 M. Yang, S. Shikita, H. Min, I. S. Park, H. Shibata, N. Amanokura and T. Yasuda, *Angew. Chem., Int. Ed.*, 2021, **60**, 23142–23147.
17 Y.-T. Lee, C.-Y. Chan, N. Matsuno, S. Uemura, S. Oda, M. Kondo, R. W. Weerasinghe, Y. Hu, G. N. I. Lestanto, Y. Tsuchiya, Y. Li, T. Hatakeyama and C. Adachi, *Nat. Commun.*, 2024, **15**, 3174.
18 W. Yuan, Q. Jin, M. Du, L. Duan and Y. Zhang, *Adv. Mater.*, 2024, **36**, 2410096.
19 L. Guo, W. Cui, L. Li, Y. Pu, K. Wang, P. Zheng, Y. Wang and C. Li, *Adv. Mater.*, 2025, **37**, 2500269.
20 Y. Pu, Q. Jin, Y. Zhang, C. Li, L. Duan and Y. Wang, *Nat. Commun.*, 2025, **16**, 332.
21 J. Liu, Y. Zhu, T. Tsuboi, C. Deng, W. Lou, D. Wang, T. Liu and Q. Zhang, *Nat. Commun.*, 2022, **13**, 4876.
22 X.-C. Fan, K. Wang, Y.-Z. Shi, Y.-C. Cheng, Y.-T. Lee, J. Yu, X.-K. Chen, C. Adachi and X.-H. Zhang, *Nat. Photonics*, 2023, **17**, 280–285.
23 X. F. Luo, S. Q. Song, H. X. Ni, H. Ma, D. Yang, D. Ma, Y. X. Zheng and J. L. Zuo, *Angew. Chem., Int. Ed.*, 2022, **61**, e202209984.
24 O. Sachnik, N. Kinaret, R. Saxena, M. Manz, W. Liu, J. T. Blaskovits, D. Andrienko, J. J. Michels, P. W. M. Blom and G.-J. A. H. Wetzelaer, *Nat. Mater.*, 2025, **24**, 1742–1748.
25 X. Cai, J. Xue, C. Li, B. Liang, A. Ying, Y. Tan, S. Gong and Y. Wang, *Angew. Chem., Int. Ed.*, 2022, **61**, e202200337.
26 P. Jiang, L. Zhan, X. Cao, X. Lv, S. Gong, Z. Chen, C. Zhou, Z. Huang, F. Ni, Y. Zou and C. Yang, *Adv. Opt. Mater.*, 2021, **9**, 2100825.
27 D. H. Ahn, S. W. Kim, H. Lee, I. J. Ko, D. Karthik, J. Y. Lee and J. H. Kwon, *Nat. Photonics*, 2019, **13**, 540–546.

28 H. Lim, H. J. Cheon, S. J. Woo, S. K. Kwon, Y. H. Kim and J. J. Kim, *Adv. Mater.*, 2020, **32**, 2004083.
29 J. U. Kim, I. S. Park, C. Y. Chan, M. Tanaka, Y. Tsuchiya, H. Nakanotani and C. Adachi, *Nat. Commun.*, 2020, **11**, 1765.
30 R. Braveenth, H. Lee, J. D. Park, K. J. Yang, S. J. Hwang, K. R. Naveen, R. Lampande and J. H. Kwon, *Adv. Funct. Mater.*, 2021, **31**, 2105805.
31 H. J. Kim, H. Kang, J. E. Jeong, S. H. Park, C. W. Koh, C. W. Kim, H. Y. Woo, M. J. Cho, S. Park and D. H. Choi, *Adv. Funct. Mater.*, 2021, **31**, 2102588.
32 H. J. Tan, G. X. Yang, Y. L. Deng, C. Cao, J. H. Tan, Z. L. Zhu, W. C. Chen, Y. Xiong, J. X. Jian, C. S. Lee and Q. X. Tong, *Adv. Mater.*, 2022, **34**, 2200537.
33 H. Lee, R. Braveenth, S. Muruganantham, C. Y. Jeon, H. S. Lee and J. H. Kwon, *Nat. Commun.*, 2023, **14**, 419.
34 S. J. Wu, X. F. Fu, D. H. Zhang, Y. F. Sun, X. Lu, F. L. Lin, L. Meng, X. L. Chen and C. Z. Lu, *Adv. Mater.*, 2024, **36**, 2401724.
35 C. Wu, W. Liu, K. Li, G. Cheng, J. Xiong, T. Teng, C. M. Che and C. Yang, *Angew. Chem., Int. Ed.*, 2021, **60**, 3994–3998.
36 Y. K. Qu, D. Y. Zhou, Q. Zheng, P. Zuo, Z. L. Che, L. S. Liao and Z. Q. Jiang, *Angew. Chem., Int. Ed.*, 2024, **63**, e202408712.
37 R. Z. An, F. M. Zhao, C. Shang, M. Zhou and L. S. Cui, *Angew. Chem., Int. Ed.*, 2025, **64**, e202420489.
38 Z. Xiao, Y. Zou, Z. Chen, J. Miao, Y. Qiu, Z. Huang, X. Cao, X. Peng and C. Yang, *Adv. Mater.*, 2025, **37**, 2419601.
39 Y. Chang, K. Zhang, L. Zhao, X. Wang, S. Wang, S. Shao and L. Wang, *Angew. Chem., Int. Ed.*, 2024, **64**, e202415607.
40 Q. Li, F. Huang, X. Xu, X. Wang, Z. Ma, Z. Quan, J. Liu, H. Tong, S. Shao and L. Wang, *Chem. Commun.*, 2025, **61**, 4864–4867.
41 G. Meng, H. Dai, Q. Wang, J. Zhou, T. Fan, X. Zeng, X. Wang, Y. Zhang, D. Yang, D. Ma, D. Zhang and L. Duan, *Nat. Commun.*, 2023, **14**, 2394.
42 Y. Lee, J. Kim, S. Lee, E. Sim and J.-I. Hong, *Chem. Eng. J.*, 2023, **476**, 146659.
43 Y. Sun, X. F. Fu, C. L. Hou, T. T. Lin, D. H. Zhang, J. Liu, J. X. Hu, F. L. Lin, L. Zhou, L. Meng, X. L. Chen and C. Z. Lu, *Angew. Chem., Int. Ed.*, 2025, **64**, e202511921.
44 CCDC 2523284: Experimental Crystal Structure Determination, 2026, DOI: 10.5517/ccdc.csd.cc2qpp8d.